Journal of Structural Biology 213 (2021) 107701

Contents lists available at ScienceDirect

Journal of Structural Biology

journal homepage: www.elsevier.com/locate/yjsbi

Structure of the *Yersinia* injectisome in intracellular host cell phagosomes revealed by cryo FIB electron tomography

Casper Berger [a], Raimond B.G. Ravelli [a], Carmen López-Iglesias [a], Mikhail Kudryashev [b,c], Andreas Diepold [d], Peter J. Peters [a,*]

[a] Maastricht Multimodal Molecular Imaging Institute, Maastricht University, The Netherlands
[b] Max Planck Institute of Biophysics, Frankfurt am Main, Germany
[c] Buchmann Institute for Molecular Life Sciences, Goethe University of Frankfurt, Germany
[d] Department of Ecophysiology, Max Planck Institute for Terrestrial Microbiology, Marburg, Germany

ARTICLE INFO

Keywords:
Type III secretion system
Cryo-electron tomography
Cryo-focused ion beam lamella
Subtomogram averaging
Yersinia enterocolitica
Bacterial adhesin YadA

ABSTRACT

Many pathogenic bacteria use the type III secretion system (T3SS), or injectisome, to secrete toxins into host cells. These protruding systems are primary targets for drug and vaccine development. Upon contact between injectisomes and host membranes, toxin secretion is triggered. How this works structurally and functionally is yet unknown. Using cryo-focused ion beam milling and cryo-electron tomography, we visualized injectisomes of *Yersinia enterocolitica* inside the phagosomes of infected human myeloid cells in a close-to-native state. We observed that a minimum needle length is required for injectisomes to contact the host membrane and bending of host membranes by some injectisomes that contact the host. Through subtomogram averaging, the structure of the entire injectisome was determined, which revealed structural differences in the cytosolic sorting platform compared to other bacteria. These findings contribute to understanding how injectisomes secrete toxins into host cells and provides the indispensable native context. The application of these cryo-electron microscopy techniques paves the way for the study of the 3D structure of infection-relevant protein complexes in host-pathogen interactions.

1. Introduction

The type III secretion system (T3SS), or injectisome, is a large bacterial transmembrane protein complex that transports effector proteins across both the bacterial and host membranes. These effector proteins manipulate host cells to promote favorable conditions for pathogenic bacteria. This makes the T3SS essential for virulence for many different human pathogens including *Salmonella, Shigella, Chlamydia* and *Yersinia* (Deng et al., 2017). To design drugs and vaccines against these pathogens, it is important to understand their structure in the most native setting (*in situ*).

The injectisome consists of a cytosolic sorting platform in the cytoplasm, a basal body spanning the inner and outer membrane, and a needle that protrudes from the bacterium. Assembly of the injectisome (Diepold and Wagner, 2014; Deng et al., 2017; Hu et al., 2020) is initiated by the formation of the export apparatus and the basal body (Kimbrough and Miller, 2000; Wagner et al., 2010; Kowal et al., 2013). Next, the cytosolic sorting platform is formed, attached to the export apparatus and the base of the basal body (Diepold et al., 2010). Subsequently, the helical needle structure is formed and elongated. When reaching the final needle length (Journet et al., 2003), the sorting platform and other key proteins switch the injectisome to secreting a protein that forms the needle tip. This fully assembled T3SS will become activated upon contact with a host membrane, after which the translocon proteins are secreted to form a pore into the host cell (VanEngelenburg and Palmer, 2008; Radics et al., 2014; Nauth et al., 2018). Finally, several effector proteins are secreted through the needle and the pore into the host cell. The sorting platform thus needs to sequentially switch between secreting needle, needle tip, translocon and effector proteins and this process needs to be strictly regulated. The mechanisms for this regulation as well as how contact of injectisome needles with host membranes triggers the secretion of substrates are largely unknown. Determining the structural states of injectisomes in contact with host membranes (likely secreting) and not in contact to host membranes (likely non-secreting) may help to reveal these mechanisms.

The structure of the injectisome has been extensively studied by

* Corresponding author.
E-mail address: pj.peters@maastrichtuniversity.nl (P.J. Peters).

https://doi.org/10.1016/j.jsb.2021.107701
Received 30 October 2020; Received in revised form 17 December 2020; Accepted 14 January 2021
Available online 4 February 2021

using biochemical purification followed by cryo-electron microscopy (cryo-EM) and single-particle analysis. This has been essential to determine the structure of the injectisome at resolutions allowing atomic model building (Marlovits et al., 2004; Worrall et al., 2016; Hu et al., 2018; Lunelli et al., 2020). However, purification of protein complexes from their native environment may cause parts of the complex to dissociate or change their structure. Indeed, single-particle structures of purified injectisomes lack several structural components, including the cytosolic sorting platform, the surrounding membranes and the peptidoglycan layer. Cryo-electron tomography (CET), however, can visualize protein complexes in their native environment. Structures of the injectisome of several species have been determined with CET including *Salmonella enterica, Shigella flexneri* and *Chlamydia trachomatis* (Kawamoto et al., 2013; Hu et al., 2015; 2017;; Nans et al., 2015; Butan et al., 2019). This revealed the structure of the cytosolic sorting platform to consist of six pod-like densities, which contrast with the ring structure found in the cytosolic C-ring of the closely related bacterial flagellar motor (Thomas et al., 2006; Chen et al., 2011; Hu et al., 2015, 2017; Makino et al., 2016). The structure of the sorting platform of *Y. enterocolitica* has not yet been determined (Kudryashev et al., 2013).

Because of the pivotal role of the T3SS during infection, determining different structural states of the injectisome during infection is critical to understand the mechanisms of substrate secretion. Indeed, contact with host cells has already been shown to result in structural differences in *C. trachomatis* minicells compared to a host-free state including a contraction of the basal body and stabilization of the sorting platform (Nans et al., 2015). In contrast, the injectisome of *S. enterica* minicells in contact with host cells did not show any structural rearrangements (Park et al., 2018). The injectisome, and in particular the sorting platform, is a highly dynamic complex, and secreting conditions have been shown to increase the exchange rate of the dynamic cytosolic injectisome subunits that form the sorting platform in *Y. enterocolitica* (Diepold et al., 2015, 2017). The structural changes in the injectisome triggered by host contact in *C. trachomatis* and the altered exchange rate of sorting platform proteins observed in *Y. enterocolitica* make it likely that structural changes occur upon contact of the needle with a host membrane.

Although *Y. enterocolitica* is considered primarily an extracellular pathogen (Devenish and Schiemann, 1981; Du et al., 2016), there is substantial evidence for intracellular survival and replication inside infected phagocytic myeloid cells, and *Y. enterocolitica* is known to gain entry through M cells of the gastrointestinal tract, where it can infect Peyer's patches (Tabrizi and Robins-Browne, 1992; Autenrieth and Firsching, 1996; Pujol and Bliska, 2005; VanCleave et al., 2017; Bohn et al., 2019). This makes myeloid cells excellent models to study injectisome structure in a biologically relevant infection context. We therefore used primary human monocytes and monocyte-derived dendritic cells to investigate with CET the injectisome structure of *Y. enterocolitica* during intracellular infection.

Whereas conventional EM sample preparation generally only allows for ultrastructural studies of host-pathogen interactions (van der Wel et al., 2007), rapid freezing and cryo-microscopy preserves the molecular structure of the cell. Only the edges of mammalian cells are thin enough for electrons to penetrate to allow imaging with CET. In order to access the areas inside the cells, we used cryo–focused ion beam (cryo-FIB) to make ~200-nm-thick lamellae of the infected cells (Marko et al., 2007; Schaffer et al., 2017). These techniques allow protein complexes to be studied in their native environment at nanometer resolution (Bykov et al., 2017; Medeiros et al., 2018; Weiss et al., 2019; Albert et al., 2020), and enabled us to study the injectisome within infected host cells.

In this work, we visualized *Y. enterocolitica* during intracellular infection of primary myeloid cells using CET on FIB-lamellae and showed that injectisome needles directly contact, and in some cases deform, host membranes. Furthermore, we observed large variability between the contact angles of individual needles with host membranes, the lengths of the needles and lengths of the basal body. A minimal injectisome needle length seems to be required to make contact with host membranes. Finally, subtomogram averaging revealed the entire structure of the injectisome of *Y. enterocolitica* during intracellular infection, including the basal body, cytosolic sorting platform and the needle tip complex. This showed structural differences in the sorting platform compared to other species. These structural data on the injectisome structure during intracellular infection pave the way towards providing the fine molecular details of how injectisomes interact with host cells under native conditions.

2. Materials and methods

2.1. Bacterial strains and culture conditions

A starter culture of *Y. enterocolitica* AD4334 (E40 ΔblaA Δasd ΔyopH ΔyopO ΔyopP ΔyopE ΔyopM ΔyopT) SctV-mCherry was grown overnight at 28 °C in 37 g/L brain heart infusion medium (BHI) containing 35 μg/ml nalidixic acid (NAL) and 80 μg/ml diaminopimelic acid (DAP). The starter culture was used to inoculate a culture at an OD_{600} of 0.12 in 37 g/L BHI containing 35 μg/ml NAL, 80 μg/ml DAP, 0.4% glycerol (v/v) and 20 mM $MgCl_2$. Bacteria were grown for 1.5 h at 28 °C to recover exponential growth, and 3 h at 37 °C to induce the expression of the T3SS.

For confirming the identity of the extracellular protein coat as YadA, we used the strain *Yersinia enterocolitica* E40 AD4053 (E40 ΔblaA Δasd ΔyopH ΔyopO ΔyopP ΔyopE ΔyopM ΔyopT ΔyadA) where expression of YadA was prevented by the integration of the mutator plasmid pJLM4031 in the the YadA gene. These bacteria were grown as described above except with 100 μg/ml of streptomycin in the culture medium.

2.2. Monocyte isolation and differentiation

Human blood buffy coat was acquired from Sanquin, and monocytes were isolated by negative selection with RosetteSep (Stemcell Technologies) as per the manufacturer's instructions. Isolated monocytes were cultured at 37 °C and 5% CO_2 in AIM V medium (Thermo Fisher Scientific, cat. 12055083) in non-tissue culture–treated petri dishes (Greiner, ref 633179) for 1 day. The medium was replaced with AIM V medium containing 25 ng/ml interleukin-4 (IL-4) (PeproTech, cat 200-04) and 200 ng/ml granulocyte–macrophage colony-stimulating factor (GM-CSF) (PeproTech, cat 300-03), and the cells were allowed to differentiate into dendritic cells for 6 days (Hiasa et al., 2009). For cryo-fluorescence microscopy, J774 macrophages were grown in RPMI 1640 medium (Thermo Fisher Scientific. Cat. 11875093) supplemented with 10% fetal bovine serum.

2.3. Infection and adhering cells to grid

Isolated monocytes or differentiated dendritic cells or J774 macrophages were washed with RPMI 1640 medium and detached by incubating for 10 min with 2 ml TripleE (Thermo Fisher Scientific cat. 12604013) followed by scraping. Then 400 000 cells were seeded in a petri dish (Greiner,ref 627160) containing 8 UltrAufoil 200-mesh R2/2 grids (Russo and Passmore, 2014), and the cells were allowed to adhere for 1 h. The cells were infected with *Y. enterocolitica* at a multiplicity of infection (MOI) of 100 for 1 h, then 10-nm gold fiducials were added. For cryo-fluorescence microscopy, an MOI of 40 was used and the nucleus was stained for 20 min with NucBlu Live ReadyProbe Reagent (Thermo Fisher, cat. R37605).

2.4. Cryo-fluorescence microscopy

Z-stacks of intra- and extracellular bacteria were imaged under cryogenic conditions with a Corrsight spinning disk confocal fluorescence microscope (Thermo Fisher Scientific) with a 40× air objective

(Zeiss, 420363-9901-000) with 405 and 561 nm excitation in spinning disk mode. Z-stacks were deconvoluted (Sage et al., 2017) and max-intensity projections were made for visualization.

2.5. Jet vitrification

EM grids were vitrified with a modified Vitrobot (Thermo Fisher Scientific), where the liquid ethane–plunging container was replaced with a custom-built jet vitrification device (Ravelli et al., 2020) and a force sensor on the blotting pads provides live feedback on the force that the blotting pads apply for more consistent blotting results. On the blotting pads, a sheet of Teflon was used on the sample side and Whatmann filter paper (Sigma-Aldrich, cat. no. 1001–055) on the backside of the grid. A blotting force of 2.45 N was used with a blotting time of 5 s, waiting time of 2 s, chamber humidity of 80% and temperature of 37 °C. Vitrified grids were clipped with autogrids (Thermo Fisher Scientific, cat. no. 1036173). Autogrids were modified with a laser mark pattern to orient the grid when loading it in the FIB/SEM and TEM microscopes.

2.6. Cryo-FIB lamella fabrication

For FIB lamella fabrication, a SCIOS FIB/SEM dual-beam (Thermo Fisher Scientific) was used that was upgraded to the functional equivalent of an Aquilos (Thermo Fisher Scientific). A thin layer of platinum was sputtered on the grid with the build-in sputter coater (6 s, 10 W, 600 V, 30 mA). MAPS software 3.1 (Thermo fisher Scientific) was used to acquire an overview of the grid, and sites of interest were selected and eucentric height for each position was determined. Organometallic platinum was deposed on three different sides on the edge of the grid for 3 s, and rectangular pattern milling was used to make FIB lamellae at 30 kV and a current between 0.05 and 1nA at a milling angle of 11° relative to the grid. The initial width of the lamella was chosen between 8 and 20 μm with lower width of the milling box in consecutive milling steps. A thin layer of platinum was sputtered over the final lamellae (3 s, 10 W, 600 V, 30 mA).

2.7. Cryo-electron tomography

Most CET was done with a Tecnai Arctica (Thermo Fisher Scientific) operating at 200 kV. Data were acquired with a Falcon III direct electron detector operating in electron counting mode with a pixel size of 2.73 Å. TEM grids with lamella were oriented 90° counterclockwise in the autoloader relative to their orientation in the FIB/SEM using the laser marks. Low-dose stitched overviews of the lamellae were acquired to determine sites of interest with the MAPS software 3.6 (Thermo Fisher Scientific). Tilt series were acquired with the Tomography software 4.9 (Thermo Fisher Scientific) with a bidirectional tilt scheme between −51° and 51° with 3° increments or −34° and 34° with 2° increments with a total dose of 100 e-/Å^2. The tilt angles were corrected for the pre-tilt of the lamella. Over 150 tilt series were collected.

For the control of the YadA mutant, tilt series were recorded with a Titan Krios operating at 300 kV and equipped with a K2 operating in electron counting mode with a pixel size of 2.72 Å and a bidirectional tilt scheme between −60° and 60° with 2° increments correcting for the pre-tilt of the lamella.

2.8. Data processing and tomogram reconstruction

Dose fractions were aligned with MotionCor2 version 1.1 (Zheng et al., 2017). Tilt series were aligned and reconstructed with Etomo version 4.9.5 (Mastronarde and Held, 2017) with fiducial-based local alignment, subtraction of gold fiducial markers and CTF correction by phase-flipping and reconstructed with weighted back projection. For selecting subtomograms, 4× binned tomograms were flipped in XY and filtered with TomDeconv (https://github.com/dtegunov/tom_deconv/) (Tegunov and Cramer, 2019). For visualization and the movies, 2× or 4× binned weighted back projection tomograms were reconstructed from tilt series where the gold fiducials were computationally removed, and the platinum layer was computationally subtracted with Masktomrec (Fernandez et al., 2016). Tomograms were flipped in XY and filtered with TomDeconv EM. Segmentation and isosurface renderings was done with Amira 4.7 (Thermo Fisher Scientific).

2.9. Subtomogram averaging

A total of 202 injectisomes were manually picked in 3DMOD (IMOD 4.9.5) (Mastronarde and Held, 2017) and Dynamo version 1.1401 (Castaño-Díez et al., 2017). Particles were extracted from 2× binned tomograms with Dynamo with a box size of 256 pixels, manually aligned with Dynamo gallery, in-plane axis rotations were randomized to reduce missing wedge artifacts, and shifts and euler angles were iteratively refined with restricted freedom. The initial reference was created by averaging the manually aligned particles. Separate masks were used to focus the alignment on the base of the needle and the basal body, or the cytosolic sorting platform and the basal body. For creating the averages during the subtomogram averaging procedure for the basal body and the cytosolic sorting platform, 141 and 101 of the particles with the highest cross-correlation score were used, respectively. C6, C3 and C5 symmetry were applied during the last steps of the refinement procedure for the sorting platform, basal body and needle tip, respectively. These symmetry values were derived from literature (Broz et al., 2007; Worrall et al., 2016; Hu et al., 2017) and by applying different rotational symmetries to the subtomogram average structures followed by visual inspection of orthogonal slices and visual inspection of the averages without applied symmetry.

To compare the structures of injectisomes contacting the host membranes (contact) to those that don't (non-contact), injectisomes were manually sorted into two different sets of particles and independently iteratively aligned with a mask covering the basal body. For the sorting platform, particles were averaged based on the computed alignments determined with all the particles. As a control, random sets of injectisomes with the same number of particles were used.

For the needle tip complex, 75 needle tip complexes of non-contact injectisomes were manually picked in Dynamo, extracted from 4× binned tomograms and manually aligned with Dynamo gallery. Subtomograms from manually refined particle coordinates were extracted from 2× binned tomograms, and in-plane axis rotations were randomized, and iterative refinement was performed in Dynamo. The initial reference was created by averaging the manually aligned particles. Forty-five particles with the highest cross-correlation score were used to create the averages during the subtomogram averaging procedure.

To determine the resolution, a Fourier-shell correlation was performed by separating the even and odd particles and independently aligning them at increasingly higher low-pass filter values. Final resolution was determined with the 0.143 criterion without symmetry and with C6, C3 and C5 symmetry for the sorting platform, basal body and needle tip, respectively.

2.10. Quantifications and statistics

For determining the basal body length, 2D slices of the aligned subtomograms were loaded into 3DMOD (IMOD version 4.9.5), and basal body length was measured with the measuring tool between the center of inner membrane to the center of the outer membrane. For measuring the length of the needles, anchor points were added to the base and the tip of the needle in dtmslice (Dynamo version 1.1401) in the tomograms, and the distance between the points was measured in 3D. An independent two-tailed, student-T test was used to compare basal body and needle lengths of injectisomes contacting the host (contact) compared to the remaining injectisomes (non-contact). The contact angle between the needle and the host membrane was measured in Fiji

with the angle tool (Schindelin et al., 2012; Rueden et al., 2017). Local thickness of the lamella was measured with the measuring tool in 3DMOD (IMOD 4.9.5) on the reconstructed tomograms in the center of the volume (Mastronarde and Held, 2017).

3. Results

3.1. Cryo-FIB and CET workflow

To study the T3SS of *Y. enterocolitica* in an intracellular host environment, we used monocytes and dendritic cells infected with *Y. enterocolitica* AD4334. This strain is no longer pathogenic to host cells, but the injectisome can still actively secrete effector proteins (Kudryashev et al., 2013; Diepold et al., 2015). We established a workflow for CET on FIB-fabricated lamellae where the cryo-FIB was used to thin down the infected cells into ~200-nm slices to enable CET of the interior of cells.

We optimized grid type, blotting, freezing and FIB-milling procedures for these samples, resulting in reproducible grid and lamellae preparation (Fig. 1). Typically, several tilt-series of intracellular bacteria were acquired on a single lamella (Fig. 1B, C). To obtain sufficient contrast at high tilt angles with a cryo-TEM, it is important to have thin lamellae. We measured the local thickness in tomograms used for subtomogram averaging in this study and found an average thickness of 186 ± 58 nm (n = 63) (Fig. 1D).

Using this workflow, we acquired over 150 tomographic tilt-series of *Y. enterocolitica* inside infected monocytes and dendritic cells using a 200-kV cryo-electron microscope. Successfully establishing a reproducible cryo-FIB and CET workflow allowed us to study the *Y. enterocolitica* injectisome in an intracellular host environment at high resolution.

3.2. Y. enterocolitica in intracellular host phagosomes

In the reconstructed tomograms, *Y. enterocolitica* was present in phagosomes of host cells. The large number of bacterial ribosomes and absence of bacterial membrane deformations suggest that the bacteria are able to maintain homeostasis inside the host phagosomes (Fig. 2, Suppl. Fig. 1). The surface of the bacteria was densely covered with protein stalks which extend 30 nm from the bacterial outer membrane with distal larger head groups (Fig. 2A and Suppl. Movie 1). We identified this protein as the adhesion molecule YadA, which was confirmed by their absence in the YadA knockout mutant (Fig. 2B) (Hoiczyk, 2000; Koiwai et al., 2016). The quality of the tomograms allows for individual trimeric ~ 200 kDa YadA protein complexes to be identified, which provides confidence for interpreting features of the injectisome in the tomograms.

We found injectisomes in many tomograms, characterized by the

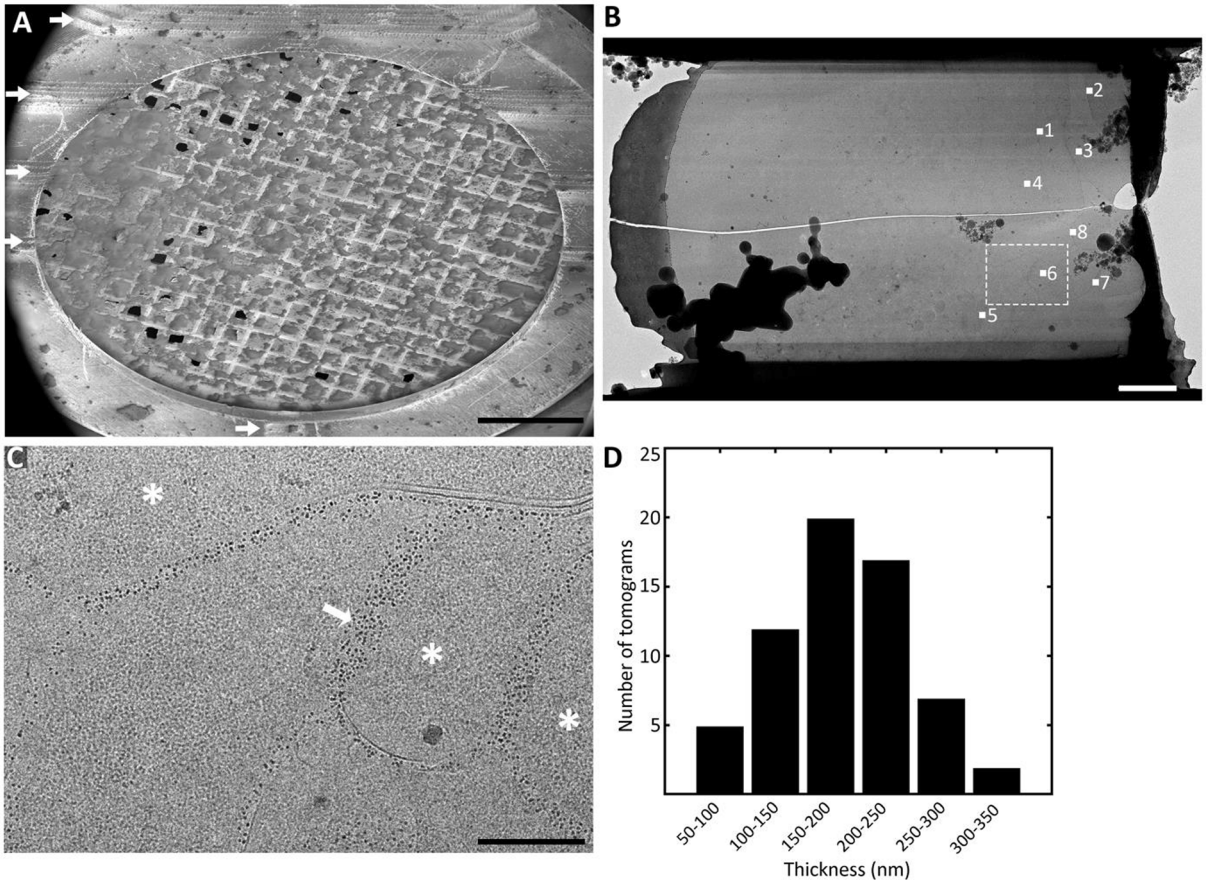

Fig. 1. Overview of the cryo–electron tomography workflow on FIB-lamellae used in this study to investigate the intracellular infection of *Y. enterocolitica*. (A) Cryo-SEM overview of a sample EM-grid on which FIB-lamellae were produced followed by cryo–electron tomography. Laser marks on the autogrid are used to orient the grid in the TEM so that the lamellae are perpendicular to the tilt axis (white arrows). Scale bar: 500 µm. (B) Stitched cryo-TEM tile scan overview of FIB-lamella to determine where to record the tilt-series. Positions and order in which the tilt-series were acquired, indicated with solid white squares and numbers, respectively. The tomogram reconstructed from the tilt-series acquired at position 6 is shown in Fig. 2D and E. Scale bar: 2 µm. Dashed white square shows the enlarged area in (C), in which several bacteria are visible inside the host cell (white star) surrounded by 10-nm gold beads (white arrow). Gold beads were used as fiducial markers for tilt-series alignment and were localized in the phagosomes since they were added during the infection. Scale bar: 500 nm. (D) Applying these steps resulted in reproducibly thin lamella with an average local thickness of 186 ± 58 nm (n = 63). Histogram shows the local thickness on lamella where all 63 tilt-series used for subtomogram averaging were acquired.

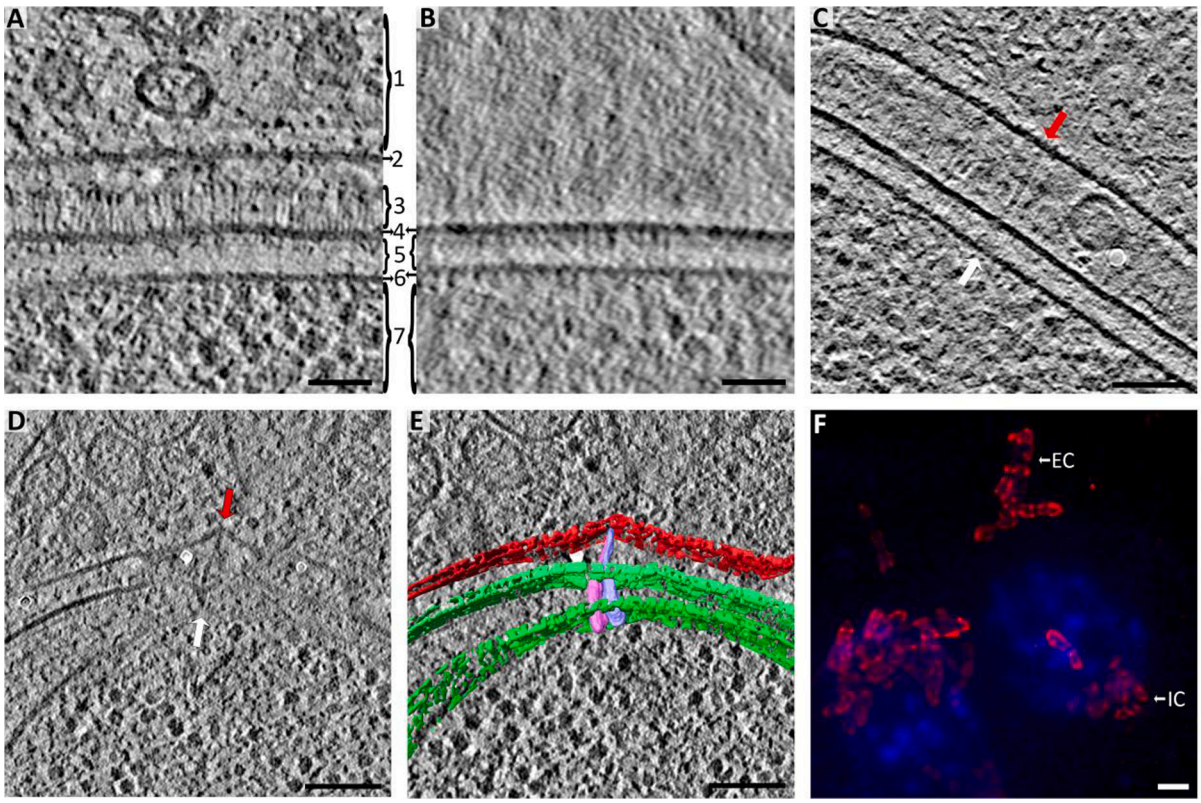

Fig. 2. Injectisomes of *Y. enterocolitica* during intracellular infection deform host membranes. (A) We observed that *Y. enterocolitica* AD4334 is densely covered in the trimeric ~200 kD autotransporter YadA (3), which extends 30 nm from the outer membrane. The bacterial outer membrane was not observed to come into contact to the phagosomal membrane and a gap of around 30 nm or greater was observed between the two. From top to bottom: 1 – host cytosol, 2 – phagosomal membrane, 3 – YadA, 4 – bacterial outer membrane, 5 – periplasm, 6 – bacterial inner membrane, 7 – bacterial cytosol. Scale bar: 50 nm. (B) The identity of the YadA proteins was confirmed with the *Y. enterocolitica* AD4053 strain, which does not express YadA. YadA has been observed on the outside of *Y. enterocolitica* previously (Hoiczyk, 2000) and its size and appearance are consistent with its structure (Koretke et al., 2006). Scale bar: 50 nm. (C) Intracellular injectisome needle of *Y. enterocolitica* interacting with the phagosomal membrane (red arrow) of the host. The injectisome is indicated by a white arrow. Scale bar: 100 nm. (D) Deformation of the host phagosomal membrane (red arrow), presumably by the injectisome needle. The injectisome is indicated by a white arrow. Scale bar: 100 nm. (E) Segmentation of the tomographic volume of panel D with the injectisome visible in panel D shown in pink and an injectisome from another tomographic slice in purple. The host phagosomal membrane (red) is deformed where the needles interact with it. Scale bar: 100 nm. (F) Cryo-fluorescence image of *Y. enterocolitica* during intracellular infection (nucleus in blue) with the injectisome export apparatus protein SctV labeled with the fluorescent protein mCherry (red). Scale bar: 3 μm.

electron-dense basal body and the needle structure protruding from the outer membrane (Fig. 2C and Suppl. Movie 2). The needle tip often interacts with membranes of the host. In some cases, the host membrane is deformed where the needle tip interacts with it (Fig. 2D, E). In some of the injectisomes that deform the host membrane, we also observed a small deformation of the bacterial cell envelope near the basal body (Suppl. Fig. 2). The injectisomes also appeared to cluster (Fig. 2E), as has been reported previously for *Y. enterocolitica* without host contact (Kudryashev et al., 2015). We used cryo-fluorescence microscopy to visualize the distribution of the injectisome clusters during infection (Fig. 2F) and did not observe a clear preferred localization to the poles or other regions of the membrane. Additionally, we did not find any differences in the distribution of the injectisomes of intracellular compared to extracellular bacteria. This similar distribution suggests that no large changes in the localization of injectisomes clusters occur upon host cell entry.

3.3. Structural heterogeneity of injectisomes

Since contact to host cells is known to promote secretion of T3SS effector proteins (VanEngelenburg and Palmer, 2008; Radics et al., 2014; Nauth et al., 2018), injectisomes where the needle tip contacts the host membrane are likely to be actively secreting. We therefore in this study compared injectisomes contacting the host membrane, and likely to be actively secreting (referred to as contact injectisomes), to injectisomes where the needle does not contact the host membrane, which are likely to be in a non-secreting state (referred to as non-contact injectisomes) (Fig. 3A).

To characterize the injectisomes *in situ* in more detail, we measured their different components, including the contact angles of injectisome needles to the host membranes as well as the lengths of the needles and basal bodies. Most needles interacted with the host membrane at angles close to 90°, but also many needles interacted at more shallow angles (Fig. 3B). We observed contact angles between 40°-90°, except for one injectisome that contacts a host vesicle (or tubular invagination) at a very shallow angle (Suppl. Fig. 3) We did not observe any needle structures protruding across the membranes, indicating piercing. The length of injectisome needles was highly variable between 11 and 171 nm (Fig. 3C). To determine whether needle length was related to interaction with the host membrane, we compared the needle lengths between contact and non-contact injectisomes. A longer mean needle length of 69 ± 25 nm was found for contact injectisomes (n = 62) compared to a mean needle length of 61 ± 31 nm for non-contact injectisomes (n = 102) (P = 0.08) (Fig. 3C). Non-contact injectisomes showed greater frequency of short (<30 nm) needles, of 12% (12 of 102) needles compared to only 3% (2 of 62) of contact injectisomes with short needles. The minimal distance between the bacterium and the phagosomal membrane is observed to be around 30 nm, which likely explains why short needles are very unlikely to bridge this gap. A minimal needle length to make host contact thus seems to be required for intracellular

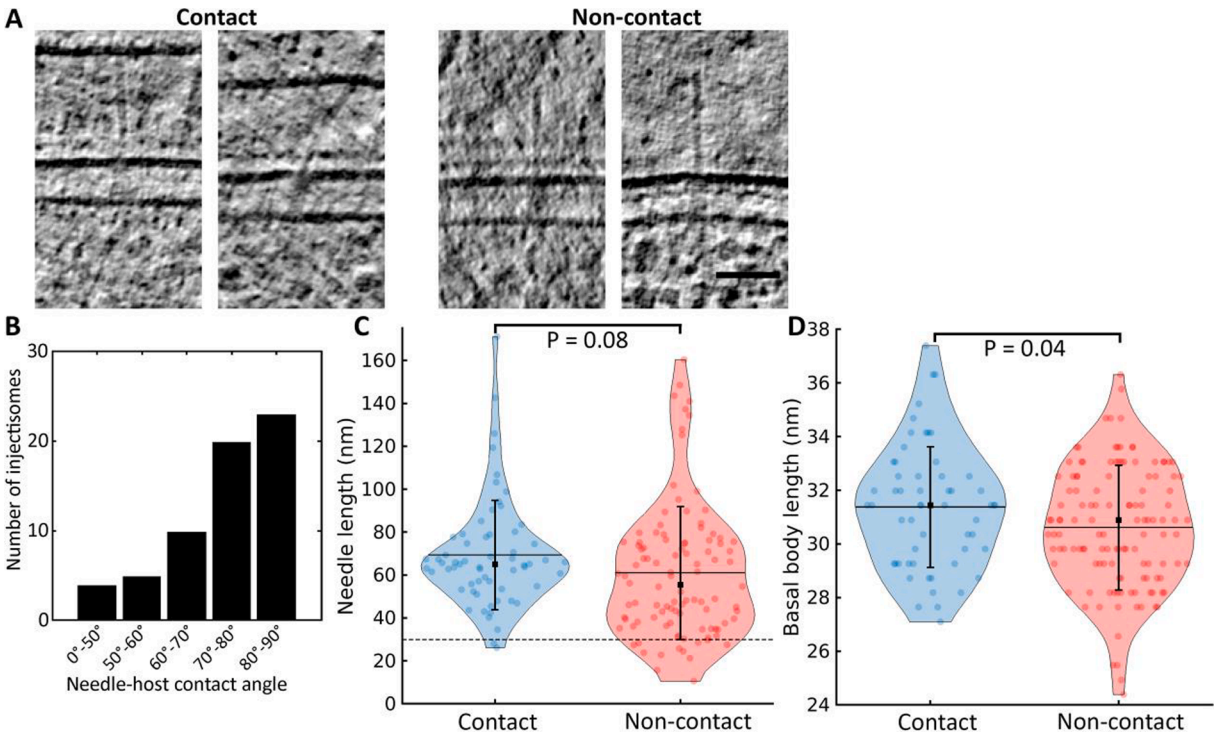

Fig. 3. Comparison of contact and non-contact injectisomes. (A) Tomographic slices showing individual injectisomes with the needle interacting with host membranes (contact) and injectisomes where the needle does not interact with host membranes (non-contact). In total, we identified 202 injectisomes, of which 122 were facing host membranes and could therefore potentially interact with it. Of these, 62 needle tips were found to interact with the host membrane. We observed large and more moderate deformations of the host membrane at seven needle–host contact sites. The needles of non-contact injectisomes were either facing another bacterium, facing the host but not making contact with it, did not have a needle or the needle tip was outside of the tomographic volume. Scale bar: 50 nm. (B) Histogram depicting the contact angles of the injectisome needles ($n = 62$) with the phagosomal membrane. (C) Violin plot comparing the distribution of the needle length of contact injectisomes (blue; mean ± SD; 69 ± 25 nm; $n = 62$) compared to non-contact injectisomes (red; mean ± SD; 61 ± 31 nm; $n = 102$). We compared the difference in needle length with a two-tailed student T-test (P = 0.08). Black horizontal lines indicate the mean and black squares the median. Error bars indicate the standard deviation from the mean. Dashed black line indicates the 30 nm minimal needle length required for host membrane contact. Of the total 202 injectisomes, we found 35 where no needle could be observed and two injectisomes where we could see a needle but could not measure its total length because it was not fully contained in the tomographic volume. (D) Violin plot showing the distribution of basal body length of contact (blue) and non-contact (red) injectisomes. Black horizontal lines indicate the mean and black dots the median. Error bars indicate the standard deviation from the mean. The average basal body length of contact injectisomes (mean ± SD; 31.4 ± 2.3 nm; $n = 56$) is significantly longer than non-contact injectisomes (mean ± SD; 30.6 ± 2.3 nm; $n = 125$) (two-tailed student T-test where P = 0.04).

injectisome attachment.

Next, we measured the basal body length of all injectisomes and compared them between contact and non-contact injectisomes (Fig. 3D, Suppl. Fig. 4). We found slightly but significantly longer basal bodies for contact injectisomes (31.4 ± 2.3 nm; $n = 56$) compared to non-contact injectisomes (30.6 ± 2.3 nm; $n = 125$) injectisomes (two-tailed student T-test where P = 0.04). The basal body length of the injectisomes was variable, as has previously been reported for the length of the basal body of *Y. enterocolitica* without host contact in minicells (Kudryashev et al., 2013).

In summary, we observed that not all needle complexes interact with the host membrane, contact angles of the needles with the host are variable and that injectisome needles can deform host membranes at their contact sites. Furthermore, we also found wide variation (11 to 171 nm) in the lengths of the injectisome needles and that a minimal needle length of ~30 nm is required to contact the host membranes. Together, these data show that the T3SS of *Y. enterocolitica* during intracellular infection is heterogeneous.

3.4. Structure of the injectisome during infection

To determine the structure of the injectisome in an intracellular infection context, we performed subtomogram averaging (Fig. 4B, Suppl. Movie 3). Because of the high flexibility in the length of the basal body, the sorting platform and the upper part of the basal body were aligned independently with different masks (Suppl. Fig. 5). A similar approach has been used previously for the type III and IV secretion systems (Kudryashev et al., 2013; Nans et al., 2015; Ghosal et al., 2017). We also separately picked the needle tips of non-contact injectisomes because of their variable lengths and angles. (Mueller et al., 2005; Broz et al., 2007). Subtomogram averaging of the needle tips of contact injectisomes did not result in stable averages because of the variable needle-membrane contact angles combined with the low number of particles (data not shown).

We applied C3 and C6 rotational symmetry to the basal body and sorting platform respectively, based on the known structure of the T3SS in *Salmonella* and *Shigella* (Worrall et al., 2016; Hu et al., 2017). It is likely that the *Yersinia* injectisome share this rotational symmetry considering the conserved interactions of proteins within the sorting platform (Jackson, 2000; Johnson and Blocker, 2008) and the shared stoichiometry between these species (Diepold et al., 2017; Zhang et al., 2017). For the needle tip, we applied C5 rotational symmetry, which has previously been determined for *Y. enterocolitica* (Mueller et al., 2005; Broz et al., 2007). The final resolutions determined by Fourier shell correlation between independently processed half-sets was 3.3 nm for the basal body, 4.0 nm for the sorting platform and 3.9 nm for the needle tip with their respective symmetry values applied (Suppl. Fig. 5).

Our structure of the basal body was similar to that determined from minicells without host contact (Kudryashev et al., 2013) (Fig. 4B). Based on the homology of the sorting platform proteins between T3SS, we

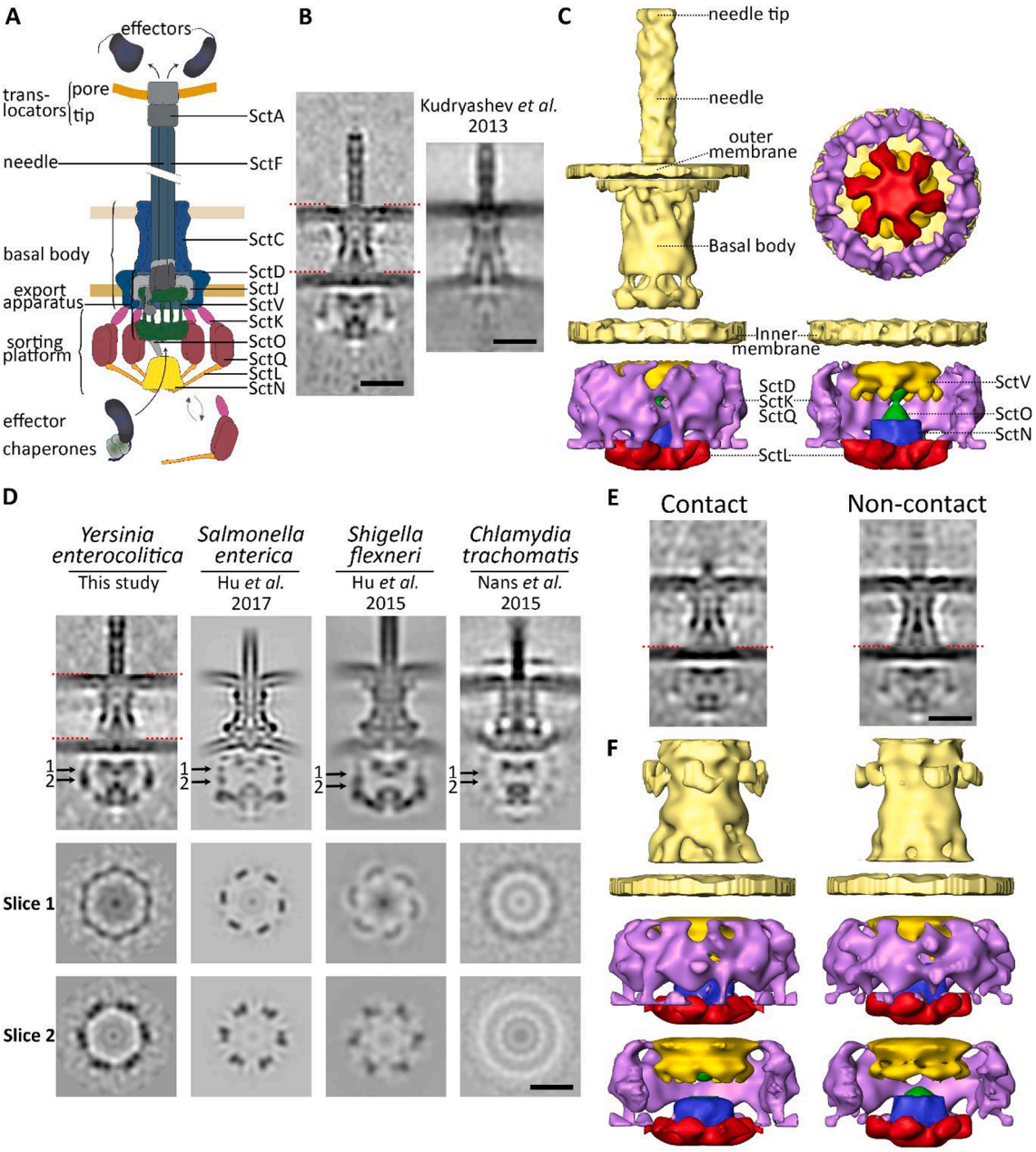

Fig. 4. Subtomogram averaging structures of the injectisome of *Y. enterocolitica* during intracellular infection of host cells. (A) Schematic overview of the main components of the injectisome (left) and the proteins (right). The basal body consists of ring structures formed by SctD and SctJ close to the inner membrane and of the secretin SctC near the outer membrane. The export apparatus spans the inner membrane into the cytosol and consists of 5 proteins including SctV (Kuhlen et al., 2018). The N-terminus of SctD extends through the inner membrane on the outside of the complex and connects via SctK to SctQ, which in turn is bound to SctL, which forms six "spokes" consisting of dimers. Directly above SctL on the inside of the sorting platform are the ATPase SctN and the stalk protein SctO. The helical needle consists of the needle protein SctF and is capped by the needle tip protein SctA. Unfolded effector proteins are secreted through the hollow needle via a pore complex formed by the translocon proteins into host cells (VanEngelenburg and Palmer, 2008; Radics et al., 2014; Nauth et al., 2018). Adapted from (Wimmi et al., 2020 Preprint). (B) Longitudinal slice of the subtomogram averages of the injectisome of *Y. enterocolitica*. The sorting platform, basal body and needle tips were aligned separately (Suppl. Fig. 5A–F) and the averages were joined (red dashed lines). Right panel: central slice of the subtomogram average previously determined in *Y. enterocolitica* (EMD 5694, (Kudryashev et al., 2013)) scaled to the average determined in this study. Scale bars: 20 nm. (C) Isosurface rendering of the average of the sorting platform with the different proteins indicated in different colors as a model for the *Y. enterocolitica* injectisome sorting platform. Right panel: bottom view of the sorting platform (top) and the sorting platform with a part of the SctQ-SctK-SctD complex removed. (D) Comparison of subtomogram average structures of different species. Density maps from The Electron Microscopy Databank were low-pass filtered to 4-nm resolution and scaled to the subtomogram average from this study. From left to right: *Y. enterocolitica* (composed of EMD-11905, EMD-11906, EMD-11907, this publication), *enterica* (EMD-8544, (Hu et al., 2017)), *S. flexneri* (EMD-2667, (Hu et al., 2015)) and *C. trachomatis* (EMD-3217, (Nans et al., 2015)). Arrows indicate positions of different orthogonal slices shown in the bottom panels. Scale bar: 20 nm. For *Y. enterocolitica*, separate subtomogram averages of the sorting platform, basal body and needle were joined together (red dashed lines). (E) Comparison of the structure of contact and non-contact injectisomes by subtomogram averages of contact injectisomes (left) and non-contact injectisomes (right) low-pass filtered to a resolution of 5 nm. The averages focused on the basal body were independently aligned and the averages for the sorting platform were created from averaging the particles based on alignments from the global average. The two subtomogram averages were joined together (red dashed line). Scale bar: 20 nm. (F) Isosurface renderings of the contact (left) and non-contact (right) injectisome structure shown in E. bottom panel: the sorting platforms with part of the SctQ-SctK-SctD complex removed.

assigned the sorting platform proteins to the measured electron densities based on the work of Hu *et al.* in *S. enterica* where they used mutants to confirm the identity of the components of the sorting platform (Hu et al., 2017) (Fig. 4A, C, D). In this model, SctD, SctK and SctQ form a 6-fold rotationally symmetric interconnected structure on the outside of the sorting platform. SctQ connects to SctL, which forms a structure with six "spokes". Just above the SctL on the inside of the sorting platform is the ATPase SctN, which connects to the stalk protein SctO that is connected to export apparatus protein SctV.

We compared our subtomogram average structure of the injectisome to those from other species and found them to be overall similar (Fig. 4D) (Hu et al., 2015, 2017; Nans et al., 2015), but also observed clear differences in the sorting platform. The diameter is conserved between all species (~29 nm), but the overall shape of the sorting platform is more rounded at the bottom for *Y. enterocolitica*, which appears to be caused by the bowl-shape formed by the SctL hexamer of dimers, whereas SctL forms a flatter structure in *S. enterica* and *S. flexneri*. Additionally, in our structure, the SctQ-SctK-SctD complex appears to form an interconnected, almost ring-like structure whereas for *S. enterica* and *S. flexneri* they form six distinct pods that are only connected by the cytosolic domains of SctD and to SctL distal from the inner membrane (Hu et al., 2015, 2017).

To determine whether substrate switching triggered by host contact results in structural changes in the injectisome, we created separate averages for contact and non-contact injectisomes focused on the basal body and the sorting platform (Fig. 4E, F) and as a control also for random sets of particles (Suppl. Fig. 6). Based on the variations observed in the random control, we conclude that no significant structural rearrangements could be observed in injectisomes in contact with the host membrane.

4. Discussion

Here we used CET on FIB-lamellae to visualize *Y. enterocolitica* during intracellular infection of myeloid cells (Fig. 1). We show that the injectisome needles can directly contact host membranes, which can result in a deformation of the host membrane (Fig. 2). We observed large heterogeneity in contact angles with the host, basal body and needle lengths of individual injectisomes, but found that needles of contact injectisomes to be elongated compared to non-contact injectisomes (Fig. 3). Finally, we determined the entire structure of the injectisomes of *Y. enterocolitica*, including the cytosolic sorting platform, inside infected monocytes and dendritic cells by using subtomogram averaging on tomograms recorded on thin cryo-FIB lamellae and found no clear structural differences in injectisomes in contact to host membranes compared to those that are not (Fig. 4).

Our observations of some *Y. enterocolitica* injectisomes deforming the host membrane and small deformations of the bacterial outer membrane (Fig. 2D, E, Suppl. Fig. 2) have also been observed for *S. enterica* (Park et al., 2018). This deformation of the bacterial envelope may suggest that a mechanical force is applied by the needle that results in a deformation of both host and bacterial membranes. Binding of adhesion proteins to host membranes has been hypothesized to provide this force by pulling closer the bacterium to enable the injectisome to contact the host (Park et al., 2018; Bohn et al., 2019). This hypothesis is supported by several studies that show a dependence of T3SS function on the bacterial adhesins YadA and Inv (Mota et al., 2005; Keller et al., 2015; Deuschle et al., 2016). However, we did not see direct interactions between the adhesion YadA and the phagosomal host membranes during intracellular infection, which may suggest that the main role of YadA in relation to T3SS function is extracellular (Keller et al., 2015). Whether deformation of host membranes is required for insertion of the translocon and/or effective secretion of effector proteins into the host cell remains to be determined. The membrane deformations may also be temporary, which could explain why they were only observed in 7 out of 62 contact injectisomes.

The contact angles of the injectisomes we measured for *Y. enterocolitica* during intracellular infection were more heterogeneous than those reported for *S. enterica*.

We observed heterogeneous contact angles between 0°–90° with over 60% of the injectisomes with contact angles of 80° or lower whereas most needle–host contact angles for *S. enterica* were reported to be close to perpendicular for wildtype bacteria, but not for mutants lacking the pore complex protein SctE or the needle tip protein SctA (Park et al., 2018). What is currently unknown is whether the contact angles remain static or whether they may change over time. Prolonged needle–host contact in a dynamic environment may create more variable contact angles over time.

In addition to the varied contact angles, we also found large variability in the injectisome needle lengths during intracellular infection. In previous studies on isolated needles from bacteria without host contact, similar mean values for needle lengths were found, but the range and variability were smaller compared to this study (Journet et al., 2003; Wagner et al., 2009). Our observed increased range and variability in needle length compared to previous studies without an infection context host may suggest that SctP, which regulates the needle length (Journet et al., 2003), may be less stringent during intracellular infection to optimize needle length locally to the variable distance of the bacterium to the phagosomal membrane. The observed minimal needle length of ~30 nm for injectisomes in contact to the host membrane is likely because shorter needles cannot bridge the >30 nm distance between the bacteria and the host. We measured a small, but statistically significant elongation of the basal body of contact injectisomes compared to non-contact. We did not observe this elongation when comparing the structure of contact and non-contact injectisomes with subtomogram averaging. The <1 nm increase in basal body length we found by measuring the heights of individual injectisomes is slightly larger than one pixel, which may explain the lack of visible differences in the averaged structures. A contraction of the basal body has previously been observed in *C. trachomatis* in contact injectisomes (Nans et al., 2015).

We determined the structure of the entire injectisome, including the cytosolic sorting platform in the context of the host cell. The sorting platform has only recently been structurally characterized because biochemical isolation disrupts its structure, and has previously not been visualized for *Yersinia*. We compared our subtomogram average structure to other species (Fig. 4D) and found that in *Y. enterocolitica* the SctQ-SctK-SctD complex appears to form an interconnected ring-like structure, which contrasts with the six pods identified in *S. enterica* and *S. flexneri*, which are only connected by the cytosolic domains of SctD and to SctL distal from the inner membrane (Hu et al., 2015, 2017). A higher resolution structure in future studies may further confirm these structural differences in the SctQ-SctK-SctD complex between *Y. enterocolitica* and other species and may also allow for molecular docking to determine which proteins and in which copy numbers form this ring-like density. Since SctQ-SctK-SctD and their orthologues in *S. enterica* have a similar molecular weight compared to *Y. enterocolitica*, this is unlikely to cause the formation of a ring-like structure rather than pod-like densities. The presence of additional proteins could better explain this difference. Studies using fluorescence light microscopy show ~22–24 copies of SctQ per injectisome in *Y. enterocolitica* and *S. enterica* (Diepold et al., 2015; Zhang et al., 2017) whereas 12 copies of SctQ per sorting platform best fit the models based on a SAXS-structure of reconstituted sorting platforms and subtomogram averaging in *S. enterica* minicells (Hu et al., 2017; Bernal et al., 2019). One explanation for the extra densities could be that there are 24 SctQ proteins per sorting platform in *Y. enterocolitica* during the conditions present in this study, with 4 SctQ proteins per "spoke" of the ring. Another possibility could be the presence of SctQc, the C-terminus of SctQ expressed as a distinct protein (Yu et al., 2011; Bzymek et al., 2012). SctQc binds in dimers to full-length SctQ (Bzymek et al., 2012; McDowell et al., 2016) and SctQc dimers bind to SctQ, SctL and SctN in a reconstituted system from isolated and overexpressed protein in solution (Bernal et al., 2019).

Moreover, SctQc has been shown to be in close proximity of injectisomes of *Y. enterocolitica* with a similar turnover as full-length SctQ (Diepold et al., 2015). A recent study reported that the C-terminal fragment of SctQ is not a structural protein of the T3SS of *S. enterica* in minicells without host contact (Lara-Tejero et al., 2019), which may reflect differences between species and/or host contact.

Whether the structural difference we observed are caused by the presence of the host or due to the differences of T3SSs between these species also remains to be determined, but the absence of structural differences observed in *S. enterica* in host contact compared to without host contact suggest a difference between the species (Hu et al., 2017; Park et al., 2018). Functionally, this structural difference may reflect differences in regulation of substrate secretion required for infecting different hosts and cell types.

When comparing the C-ring of the injectisome to the C-ring of the flagellar motor complex, the diameter of the injectisome C-ring appears to be conserved between species (~29 nm) whereas large variability in the diameter of the C-ring (34–57 nm) has been observed between different species (Rossmann and Beeby, 2018). This difference in variability in the C-ring structure is likely a reflection of its function; the flagellar C-ring's acts as a rotor to transmit torque to the central axial drive shaft for bacteria that live in surroundings with a different viscosity whereas the C-ring of the injectisome is involved in regulating substrate export into host cells. More subtle structural variations may be sufficient for optimal injectisome function in bacteria with different host and tissue tropisms.

It is striking that the inner membrane of previously published subtomogram averaging structures of *S. enterica*, *S. flexneri* and *Y. enterocolitica* have a strong inward curvature (Kudryashev et al., 2013; Hu et al., 2015, 2017), whereas the subtomogram averages in this study show an inner membrane that is nearly flat. We believe that this difference is the result of the use of minicells, which are primarily used in the previously reported T3SS structures. In contrast, in this study we used regular-sized bacteria, which are larger and have a lower membrane curvature on most of their surface.

Our finding that the structures of contact and non-contact injectisomes by subtomogram averaging did not harbor major differences is interesting. This suggests that no large structural rearrangements are triggered upon contacting the host membrane. However, it is still likely that assembled injectisomes can exist in multiple structural states, with small structural differences, considering that when the needle contacts host membranes, a signal needs to be transmitted to the export apparatus and sorting platform to initiate substrate switching. Structural rearrangements in the sorting platform could help regulate this process by allowing different chaperone-bound substrates to bind to initiate secretion (Deng et al., 2017). Also the dynamic turnover of proteins of the injectisomes and structural differences observed during host contact with CET support the existence of multiple structural states (Diepold et al., 2015, 2017; Nans et al., 2015). Classification of injectisomes into multiple conformational intermediates at a higher resolution could reveal these small structural differences in the context of the host cell, giving insights into the detailed mechanism of the injectisome function. This may become feasible in the near future, considering the rapid development in the CET field in throughput and resolution (O'Reilly et al., 2020; Zachs et al., 2020).

In conclusion, this work presents the first structure of the entire *Y. enterocolitica* injectisome in host cell phagosomes, revealing structural differences in the sorting platform compared to other species. The absence of large structural differences between injectisomes in contact with host membranes and injectisomes not in contact to host membranes suggests that activation by host contact does not trigger large structural rearrangements in the injectisome. This is an important step towards understanding how the T3SS of *Y. enterocolitica* functions *in situ* in intracellular infection in host cells. Studying the injectisome intracellularly with CET was enabled by employing cryo-FIB to prepare thin lamellae of infected cells. This method may be used to study intracellular host–pathogen interactions and the different structural states of protein complexes in their native cellular context to bridge the gap between structural and cell biology.

5. Accession numbers

The subtomogram averages of the sorting platform, basal body and the needle have been deposited in the Electron Microscopy Database with accession numbers: EMD-11905 (sorting platform), EMD-11906 (basal body) EMD-11907 (needle).

Funding

The UM acknowledge co-funding by the PPP Allowance made available by Health ~ Holland, Top Sector Life Sciences & Health, to stimulate public–private partnerships, under project number LHSM18067, as well as from the Netherlands Organisation for Scientific Research (NWO) in the framework of the National Roadmap NEMI project number 184.034.014. Misha Kudryashev is supported by the Sofja Kovalevskaja Award from the Alexander von Humbold Foundation. Andreas Diepold is supported by the Max Planck Society.

CRediT authorship contribution statement

Casper Berger: Conceptualization, Investigation, Writing - original draft. **Raimond B.G. Ravelli:** Writing - review & editing. **Carmen López-Iglesias:** Writing - review & editing. **Mikhail Kudryashev:** Writing - review & editing. **Andreas Diepold:** Conceptualization, Writing - review & editing. **Peter J. Peters:** Conceptualization, Writing - review & editing.

Declaration of Competing Interest

The authors declare that they have no known competing financial interests or personal relationships that could have appeared to influence the work reported in this paper.

Acknowledgements

We thank the Microscopy CORE Lab members for their technical and logistics support and we thank Hang Nguyen, Navya Premaraj and Nynke van Polanen for critical reading of the manuscript. We also thank Ruud Schampers and Thomas Hoffman for their technical assistance with data acquisition with the Titan Krios at The Netherlands Centre for Electron Nanoscopy.

Appendix A. Supplementary data

Supplementary data to this article can be found online at https://doi.org/10.1016/j.jsb.2021.107701.

References

Albert, S., Wietrzynski, W., Lee, C.-W., Schaffer, M., Beck, F., Schuller, J.M., Salomé, P. A., Plitzko, J.M., Baumeister, W., Engel, B.D., 2020. Direct visualization of degradation microcompartments at the ER membrane. Proc. Natl. Acad. Sci. 117 (2), 1069–1080. https://doi.org/10.1073/pnas.1905641117.

Autenrieth, I.B., Firsching, R., 1996. Penetration of M cells and destruction of Peyer's patches by Yersinia enterocolitica: an ultrastructural and histological study. J. Med. Microbiol. 44 (4), 285–294. https://doi.org/10.1099/00222615-44-4-285.

Bernal, I., Börnicke, J., Heidemann, J., Svergun, D., Horstmann, J.A., Erhardt, M., Tuukkanen, A., Uetrecht, C., Kolbe, M., 2019. Molecular organization of soluble type III secretion system sorting platform complexes. J. Mol. Biol. 431 (19), 3787–3803. https://doi.org/10.1016/j.jmb.2019.07.004.

Bohn, E., Sonnabend, M., Klein, K., Autenrieth, I.B., 2019. Bacterial adhesion and host cell factors leading to effector protein injection by type III secretion system. Int. J. Med. Microbiol. 309 (5), 344–350. https://doi.org/10.1016/j.ijmm.2019.05.008.

Broz, P., Mueller, C.A., Müller, S.A., Philippsen, A., Sorg, I., Engel, A., Cornelis, G.R., 2007. Function and molecular architecture of the Yersinia injectisome tip complex.

Mol. Microbiol. 65 (5), 1311–1320. https://doi.org/10.1111/mmi.2007.65.issue-510.1111/j.1365-2958.2007.05871.x.
Butan, C., Lara-Tejero, M., Li, W., Liu, J., Galán, J.E., 2019. High-resolution view of the type III secretion export apparatus in situ reveals membrane remodeling and a secretion pathway. Proc. Natl. Acad. Sci. 116 (49), 24786–24795. https://doi.org/10.1073/pnas.1916331116.
Bykov, Y.S., Schaffer, M., Dodonova, S.O., Albert, S., Plitzko, J.M., Baumeister, W., Engel, B.D., Briggs, J.A., 2017. The structure of the COPI coat determined within the cell. Elife 6, e32493. doi: 10.7554/eLife.32493.
Bzymek, K.P., Hamaoka, B.Y., Ghosh, P., 2012. Two translation products of yersinia yscQ assemble to form a complex essential to type III secretion. Biochemistry 51 (8), 1669–1677. https://doi.org/10.1021/bi201792p.
Castaño-Díez, D., Kudryashev, M., Stahlberg, H., 2017. Dynamo catalogue: geometrical tools and data management for particle picking in subtomogram averaging of cryo-electron tomograms. J. Struct. Biol. 197 (2), 135–144. https://doi.org/10.1016/j.jsb:2016.06.005.
Chen, S., Beeby, M., Murphy, G.E., Leadbetter, J.R., Hendrixson, D.R., Briegel, A., Li, Z., Shi, J., Tocheva, E.I., Müller, A., Dobro, M.J., Jensen, G.J., 2011. Structural diversity of bacterial flagellar motors. EMBO J. 30, 2972–2981. https://doi.org/10.1038/emboj.2011.186.
Deng, W., Marshall, N.C., Rowland, J.L., McCoy, J.M., Worrall, L.J., Santos, A.S., Strynadka, N.C.J., Finlay, B.B., 2017. Assembly, structure, function and regulation of type III secretion systems. Nat. Rev. Microbiol. 15 (6), 323–337. https://doi.org/10.1038/nrmicro.2017.20.
Deuschle, E., Keller, B., Siegfried, A., Manncke, B., Spaeth, T., Köberle, M., Drechsler-Hake, D., Reber, J., Böttcher, R.T., Autenrieth, S.E., Autenrieth, I.B., Bohn, E., Schütz, M., 2016. Role of β1 integrins and bacterial adhesins for Yop injection into leukocytes in Yersinia enterocolitica systemic mouse infection. Int. J. Med. Microbiol. 306 (2), 77–88. https://doi.org/10.1016/j.ijmm.2015.12.001.
Devenish, J.A., Schiemann, D.A., 1981. HeLa cell infection by Yersinia enterocolitica: evidence for lack of intracellular multiplication and development of a new procedure for quantitative expression of infectivity. Infect. Immun. 32, 48–55. https://doi.org/10.1128/IAI.32.1.48-55.1981.
Diepold, A., Amstutz, M., Abel, S., Sorg, I., Jenal, U., Cornelis, G.R., 2010. Deciphering the assembly of the Yersinia type III secretion injectisome. EMBO J. 29 (11), 1928–1940. https://doi.org/10.1038/emboj.2010.84.
Diepold, A., Kudryashev, M., Delalez, N.J., Berry, R.M., Armitage, J.P., Stock, A.M., 2015. Composition, formation, and regulation of the cytosolic C-ring, a dynamic component of the type III secretion injectisome. PLOS Biol. 13 (1), e1002039. https://doi.org/10.1371/journal.pbio.1002039.
Diepold, A., Sezgin, E., Huseyin, M., Mortimer, T., Eggeling, C., Armitage, J.P., 2017. A dynamic and adaptive network of cytosolic interactions governs protein export by the T3SS injectisome. Nat. Commun. 8, 15940. https://doi.org/10.1038/ncomms15940.
Diepold, A., Wagner, S., 2014. Assembly of the bacterial type III secretion machinery. FEMS Microbiol. Rev. 38 (4), 802–822. https://doi.org/10.1111/1574-6976.12061.
Du, J., Reeves, A.Z., Klein, J.A., Twedt, D.J., Knodler, L.A., Lesser, C.F., 2016. The type III secretion system apparatus determines the intracellular niche of bacterial pathogens. Proc. Natl. Acad. Sci. 113 (17), 4794–4799. https://doi.org/10.1073/pnas.1520699113.
Fernandez, J.-J., Laugks, U., Schaffer, M., Bäuerlein, F.B., Khoshouei, M., Baumeister, W., Lucic, V., 2016. Removing Contamination-Induced Reconstruction Artifacts from Cryo-electron Tomograms. Biophys. J. 110 (4), 850–859. https://doi.org/10.1016/j.bpj.2015.10.043.
Ghosal, D., Chang, Y., Jeong, K.C., Vogel, J.P., Jensen, G.J., 2017. In situ structure of the Legionella Dot/Icm type IV secretion system by electron cryotomography. EMBO Rep. 18, 726–732. https://doi.org/10.15252/embr.201643598.
Hiasa, M., Abe, M., Nakano, A., Oda, A., Amou, H., Kido, S., Takeuchi, K., Kagawa, K., Yata, K., Hashimoto, T., Ozaki, S., Asaoka, K., Tanaka, E., Moriyama, K., Matsumoto, T., 2009. GM-CSF and IL-4 induce dendritic cell differentiation and disrupt osteoclastogenesis through M-CSF receptor shedding by up-regulation of TNF-α converting enzyme (TACE). Blood 114, 4517–4526. https://doi.org/10.1182/blood-2009-04-215020.
Hoiczyk, E., 2000. Structure and sequence analysis of Yersinia YadA and Moraxella UspAs reveal a novel class of adhesins. EMBO J. 19, 5989–5999. https://doi.org/10.1093/emboj/19.22.5989.
Hu, B.o., Lara-Tejero, M., Kong, Q., Galán, J.E., Liu, J., 2017. In situ molecular architecture of the Salmonella type III secretion machine. Cell 168 (6), 1065–1074. e10. https://doi.org/10.1016/j.cell.2017.02.022.
Hu, B.o., Morado, D.R., Margolin, W., Rohde, J.R., Arizmendi, O., Picking, W.L., Picking, W.D., Liu, J., 2015. Visualization of the type III secretion sorting platform of Shigella flexneri. Proc. Natl. Acad. Sci. 112 (4), 1047–1052. https://doi.org/10.1073/pnas.1411610112.
Hu, J., Worrall, L.J., Hong, C., Vuckovic, M., Atkinson, C.E., Caveney, N., Yu, Z., Strynadka, N.C.J., 2018. Cryo-EM analysis of the T3S injectisome reveals the structure of the needle and open secretin. Nat. Commun. 9, 3840. https://doi.org/10.1038/s41467-018-06298-8.
Hu, J., Worrall, L.J., Strynadka, N.C., 2020. Towards capture of dynamic assembly and action of the T3SS at near atomic resolution. Curr. Opin. Struct. Biol. 61, 71–78. https://doi.org/10.1016/j.sbi.2019.10.005.
Jackson, M., 2000. Interactions between type III secretion apparatus components from Yersinia pestis detected using the yeast two-hybrid system. FEMS Microbiol. Lett. 186, 85–90. https://doi.org/10.1016/S0378-1097(00)00121-X.
Johnson, S., Blocker, A., 2008. Characterization of soluble complexes of the Shigella flexneri type III secretion system ATPase. FEMS Microbiol. Lett. 286, 274–278. https://doi.org/10.1111/j.1574-6968.2008.01284.x.
Journet, L., Agrain, C., Broz, P., Cornelis, G.R., 2003. The Needle Length of Bacterial Injectisomes Is Determined by a Molecular Ruler. Science 302, 1757–1760. https://doi.org/10.1126/science.1091422.
Kawamoto, A., Morimoto, Y.V., Miyata, T., Minamino, T., Hughes, K.T., Kato, T., Namba, K., 2013. Common and distinct structural features of Salmonella injectisome and flagellar basal body. Sci. Rep. 3, 3369. https://doi.org/10.1038/srep03369.
Keller, B., Mühlenkamp, M., Deuschle, E., Siegfried, A., Mössner, S., Schade, J., Griesinger, T., Katava, N., Braunsdorf, C., Fehrenbacher, B., Jiménez-Soto, L.F., Schaller, M., Haas, R., Genth, H., Retta, S.F., Meyer, H., Böttcher, R.T., Zent, R., Schütz, M., Autenrieth, I.B., Bohn, E., 2015. Yersinia enterocolitica exploits different pathways to accomplish adhesion and toxin injection into host cells. Cell. Microbiol. 17 (8), 1179–1204. https://doi.org/10.1111/cmi.12429.
Kimbrough, T.G., Miller, S.I., 2000. Contribution of Salmonella typhimurium type III secretion components to needle complex formation. Proc. Natl. Acad. Sci. 97 (20), 11008–11013. https://doi.org/10.1073/pnas.200209497.
Koiwai, K., Hartmann, M.D., Linke, D., Lupas, A.N., Hori, K., 2016. Structural basis for toughness and flexibility in the C-terminal passenger domain of an acinetobacter trimeric autotransporter adhesin. J. Biol. Chem. 291 (8), 3705–3724. https://doi.org/10.1074/jbc.M115.701698.
Koretke, K.K., Szczesny, P., Gruber, M., Lupas, A.N., 2006. Model structure of the prototypical non-fimbrial adhesin YadA of Yersinia enterocolitica. J. Struct. Biol. 155 (2), 154–161. https://doi.org/10.1016/j.jsb:2006.03.012.
Kowal, J., Chami, M., Ringler, P., Müller, S., Kudryashev, M., Castaño-Díez, D., Amstutz, M., Cornelis, G., Stahlberg, H., Engel, A., 2013. Structure of the dodecameric yersinia enterocolitica secretin YscC and its trypsin-resistant core. Structure 21 (12), 2152–2161. https://doi.org/10.1016/j.str.2013.09.012.
Kudryashev, M., Diepold, A., Amstutz, M., Armitage, J.P., Stahlberg, H., Cornelis, G.R., 2015. Yersinia enterocolitica type III secretion injectisomes form regularly spaced clusters, which incorporate new machines upon activation. Mol. Microbiol. 95, 875–884. https://doi.org/10.1111/mmi.12908.
Kudryashev, M., Stenta, M., Schmelz, S., Amstutz, M., Wiesand, U., Castaño-Díez, D., Degiacomi, M.T., Münnich, S., Bleck, C.K., Kowal, J., Diepold, A., Heinz, D.W., Dal Peraro, M., Cornelis, G.R., Stahlberg, H., 2013. In situ structural analysis of the Yersinia enterocolitica injectisome. Elife 2, e00792. doi: 10.7554/eLife.00792.
Kuhlen, L., Abrusci, P., Johnson, S., Gault, J., Deme, J., Caesar, J., Dietsche, T., Mebrhatu, M.T., Ganief, T., Macek, B., Wagner, S., Robinson, C.V., Lea, S.M., 2018. Structure of the core of the type III secretion system export apparatus. Nat. Struct. Mol. Biol. 25 (7), 583–590. https://doi.org/10.1038/s41594-018-0086-9.
Lara-Tejero, M., Qin, Z., Hu, B.o., Butan, C., Liu, J., Galán, J.E., Hughes, K.T., 2019. Role of SpaO in the assembly of the sorting platform of a Salmonella type III secretion system. PLOS Pathog. 15 (1), e1007565. https://doi.org/10.1371/journal.ppat.1007565.
Lunelli, M., Kamprad, A., Bürger, J., Mielke, T., Spahn, C.M.T., Kolbe, M., Kubori, T., 2020. Cryo-EM structure of the Shigella type III needle complex. PLOS Pathog. 16 (2), e1008263. https://doi.org/10.1371/journal.ppat.1008263.
Makino, F., Shen, D., Kajimura, N., Kawamoto, A., Pissaridou, P., Oswin, H., Pain, M., Murillo, I., Namba, K., Blocker, A.J., 2016. The architecture of the cytoplasmic region of type III secretion systems. Sci. Rep. 6, 33341. https://doi.org/10.1038/srep33341.
Marko, M., Hsieh, C., Schalek, R., Frank, J., Mannella, C., 2007. Focused-ion-beam thinning of frozen-hydrated biological specimens for cryo-electron microscopy. Nat. Methods 4 (3), 215–217. https://doi.org/10.1038/nmeth1014.
Marlovits, T.C., Kubori, T., Sukhan, A., Thomas, D.R., Galan, J.E., Unger, V.M., 2004. Structural insights into the assembly of the type III secretion needle complex. Science 306, 1040–1042. https://doi.org/10.1126/science.1102610.
Mastronarde, D.N., Held, S.R., 2017. Automated tilt series alignment and tomographic reconstruction in IMOD. J. Struct. Biol. 197 (2), 102–113. https://doi.org/10.1016/j.jsb:2016.07.011.
McDowell, M.A., Marcoux, J., McVicker, G., Johnson, S., Fong, Y.H., Stevens, R., Bowman, L.A.H., Degiacomi, M.T., Yan, J., Wise, A., Friede, M.E., Benesch, J.L.P., Deane, J.E., Tang, C.M., Robinson, C.V., Lea, S.M., 2016. Characterisation of Shigella Spa33 and Thermotoga FliM/N reveals a new model for C-ring assembly in T3SS. Mol. Microbiol. 99, 749–766. https://doi.org/10.1111/mmi.13267.
Medeiros, J.M., Böck, D., Pilhofer, M., 2018. Imaging bacteria inside their host by cryo-focused ion beam milling and electron cryotomography. Curr. Opin. Microbiol. 43, 62–68. https://doi.org/10.1016/j.mib.2017.12.006.
Mota, L.J., Mota, J., Journet, L., Sorg, I., Agrain, C., Cornelis, G.R., 2005. Bacterial Injectisomes: Needle Length Does Matter. Science 307, 1278–1278. doi: 10.1126/science.1107679.
Mueller, C.A., Broz, P., Muller, S.A., Ringler, P., Erne-Brand, F., Sorg, I., Kuhn, M., Engel, A., Cornelis, G.R., 2005. The V-antigen of yersinia forms a distinct structure at the tip of injectisome needles. Science 310, 674–676. https://doi.org/10.1126/science.1118476.
Nans, A., Kudryashev, M., Saibil, H.R., Hayward, R.D., 2015. Structure of a bacterial type III secretion system in contact with a host membrane in situ. Nat. Commun. 6, 10114. https://doi.org/10.1038/ncomms10114.
Nauth, T., Huschka, F., Schweizer, M., Bosse, J.B., Diepold, A., Failla, A.V., Steffen, A., Stradal, T.E.B., Wolters, M., Aepfelbacher, M., Coombes, B.K., 2018. Visualization of translocons in Yersinia type III protein secretion machines during host cell infection. PLOS Pathog. 14 (12), e1007527. https://doi.org/10.1371/journal.ppat.1007527.
O'Reilly, F.J., Xue, L., Graziadei, A., Sinn, L., Lenz, S., Tegunov, D., Blötz, C., Singh, N., Hagen, W.J.H., Cramer, P., Stülke, J., Mahamid, J., Rappsilber, J., 2020. In-cell architecture of an actively transcribing-translating expressome. Science 369 (6503), 554–557. https://doi.org/10.1126/science:abb3758.

Park, D., Lara-Tejero, M., Waxham, M.N., Li, W., Hu, B., Galán, J.E., Liu, J., 2018. Visualization of the type III secretion mediated Salmonella–host cell interface using cryo-electron tomography. Elife 7, 1–15. doi: 10.7554/eLife.39514.

Pujol, C., Bliska, J.B., 2005. Turning Yersinia pathogenesis outside in: subversion of macrophage function by intracellular yersiniae. Clin. Immunol. 114, 216–226. doi: 10.1016/j.clim.2004.07.013.

Radics, J., Königsmaier, L., Marlovits, T.C., 2014. Structure of a pathogenic type 3 secretion system in action. Nat. Struct. Mol. Biol. 21 (1), 82–87. https://doi.org/10.1038/nsmb.2722.

Ravelli, R.B.G., Nijpels, F.J.T., Henderikx, R.J.M., Weissenberger, G., Thewessem, S., Gijsbers, A., Beulen, B.W.A.M.M., López-Iglesias, C., Peters, P.J., 2020. Cryo-EM structures from sub-nl volumes using pin-printing and jet vitrification. Nat. Commun. 11, 2563. https://doi.org/10.1038/s41467-020-16392-5.

Rossmann, F.M., Beeby, M., 2018. Insights into the evolution of bacterial flagellar motors from high-throughput in situ electron cryotomography and subtomogram averaging. Acta Crystallogr. Sect. D Struct. Biol. 74 (6), 585–594. https://doi.org/10.1107/S2059798318007945.

Rueden, C.T., Schindelin, J., Hiner, M.C., DeZonia, B.E., Walter, A.E., Arena, E.T., Eliceiri, K.W., 2017. Image J2: ImageJ for the next generation of scientific image data. BMC Bioinformatics 18, 529. https://doi.org/10.1186/s12859-017-1934-z.

Russo, C.J., Passmore, L.A., 2014. Ultrastable gold substrates for electron cryomicroscopy. Science 346 (6215), 1377–1380. https://doi.org/10.1126/science.1259530.

Sage, D., Donati, L., Soulez, F., Fortun, D., Schmit, G., Seitz, A., Guiet, R., Vonesch, C., Unser, M., 2017. DeconvolutionLab2: An open-source software for deconvolution microscopy. Methods 115, 28–41. https://doi.org/10.1016/j.ymeth.2016.12.015.

Schaffer, M., Mahamid, J., Engel, B.D., Laugks, T., Baumeister, W., Plitzko, J.M., 2017. Optimized cryo-focused ion beam sample preparation aimed at in situ structural studies of membrane proteins. J. Struct. Biol. 197 (2), 73–82. https://doi.org/10.1016/j.jsb:2016.07.010.

Schindelin, J., Arganda-Carreras, I., Frise, E., Kaynig, V., Longair, M., Pietzsch, T., Preibisch, S., Rueden, C., Saalfeld, S., Schmid, B., Tinevez, J.-Y., White, D.J., Hartenstein, V., Eliceiri, K., Tomancak, P., Cardona, A., 2012. Fiji: an open-source platform for biological-image analysis. Nat. Methods 9 (7), 676–682. https://doi.org/10.1038/nmeth.2019.

Tabrizi, S.N., Robins-Browne, R.M., 1992. Influence of a 70 kilobase virulence plasmid on the ability of Yersinia enterocolitica to survive phagocytosis in vitro. Microb. Pathog. 13 (3), 171–179. https://doi.org/10.1016/0882-4010(92)90018-J.

Tegunov, D., Cramer, P., 2019. Real-time cryo-electron microscopy data preprocessing with Warp. Nat. Methods 16 (11), 1146–1152. https://doi.org/10.1038/s41592-019-0580-y.

Thomas, D.R., Francis, N.R., Xu, C., DeRosier, D.J., 2006. The three-dimensional structure of the flagellar rotor from a clockwise-locked mutant of Salmonella enterica Serovar Typhimurium. J. Bacteriol. 188 (20), 7039–7048. https://doi.org/10.1128/JB.00552-06.

van der Wel, N., Hava, D., Houben, D., Fluitsma, D., van Zon, M., Pierson, J., Brenner, M., Peters, P.J., 2007. M. tuberculosis and M. leprae translocate from the phagolysosome to the cytosol in myeloid cells. Cell 129 (7), 1287–1298. https://doi.org/10.1016/j.cell.2007.05.059.

VanCleave, T.T., Pulsifer, A.R., Connor, M.G., Warawa, J.M., Lawrenz, M.B., 2017. Impact of gentamicin concentration and exposure time on intracellular Yersinia pestis. Front. Cell. Infect. Microbiol. 7, 505. https://doi.org/10.3389/fcimb.2017.00505.

VanEngelenburg, S.B., Palmer, A.E., 2008. Quantification of real-time salmonella effector type III secretion kinetics reveals differential secretion rates for SopE2 and SptP. Chem. Biol. 15 (6), 619–628. https://doi.org/10.1016/j.chembiol.2008.04.014.

Wagner, S., Königsmaier, L., Lara-Tejero, M., Lefebre, M., Marlovits, T.C., Galán, J.E., 2010. Organization and coordinated assembly of the type III secretion export apparatus. Proc. Natl. Acad. Sci. 107 (41), 17745–17750. https://doi.org/10.1073/pnas.1008053107.

Wagner, S., Sorg, I., Degiacomi, M., Journet, L., Peraro, M.D., Cornelis, G.R., 2009. The helical content of the YscP molecular ruler determines the length of the Yersinia injectisome. Mol. Microbiol. 71, 692–701. https://doi.org/10.1111/j.1365-2958.2008.06556.x.

Weiss, G.L., Kieninger, A.-K., Maldener, I., Forchhammer, K., Pilhofer, M., 2019. Structure and function of a bacterial gap junction analog. Cell 178 (2), 374–384.e15. https://doi.org/10.1016/j.cell.2019.05.055.

Wimmi, S., Balinovic, A., Jeckel, H., Selinger, L., Lampaki, D., 2020. Dynamic relocalization of the cytosolic type III secretion system components prevents premature protein secretion at low external pH. bioRxiv 869214. doi: doi.org/10.1101/869214.

Worrall, L.J., Hong, C., Vuckovic, M., Deng, W., Bergeron, J.R.C., Majewski, D.D., Huang, R.K., Spreter, T., Finlay, B.B., Yu, Z., Strynadka, N.C.J., 2016. Near-atomic-resolution cryo-EM analysis of the Salmonella T3S injectisome basal body. Nature 540 (7634), 597–601. https://doi.org/10.1038/nature20576.

Yu, X.-J., Liu, M., Matthews, S., Holden, D.W., 2011. Tandem translation generates a chaperone for the Salmonella type III secretion system protein SsaQ. J. Biol. Chem. 286 (41), 36098–36107. https://doi.org/10.1074/jbc.M111.278663.

Zachs, T., Schertel, A., Medeiros, J., Weiss, G.L., Hugener, J., Matos, J., Pilhofer, M., 2020. Fully automated, sequential focused ion beam milling for cryo-electron tomography. Elife 9, 1–14. https://doi.org/10.7554/eLife.52286.

Zhang, Y., Lara-Tejero, M., Bewersdorf, J., Galán, J.E., 2017. Visualization and characterization of individual type III protein secretion machines in live bacteria. Proc. Natl. Acad. Sci. U.S.A. 114 (23), 6098–6103. https://doi.org/10.1073/pnas.1705823114.

Zheng, S.Q., Palovcak, E., Armache, J.-P., Verba, K.A., Cheng, Y., Agard, D.A., 2017. MotionCor2: anisotropic correction of beam-induced motion for improved cryo-electron microscopy. Nat. Methods 14 (4), 331–332. https://doi.org/10.1038/nmeth.4193.